



Stability and magnetic behavior of exfoliable nanowire one-dimensional materialsJoshua T. Paul , Janet Lu, Sohun Shah, Stephen R. Xie , and Richard G. Hennig**Department of Materials Science and Engineering, University of Florida, Gainesville, Florida 32611, USA
and Quantum Theory Project, University of Florida, Gainesville, Florida 32611, USA*

(Received 9 December 2022; accepted 17 May 2023; published 26 July 2023)

Low-dimensional materials can display enhanced electronic, magnetic, and quantum properties. We use the topological scaling algorithm to identify all sufficiently metastable materials in the Materials Project database to identify bulk crystals with one-dimensional (1D) structural motifs: Five hundred fifty-one crystals that are within 50 meV atom⁻¹ of the thermodynamic hull display 1D motifs, where 293 of these contain *d*-valence elements, which we focus on in this work. After exfoliating nanowires from 263 of these materials and calculating their thermodynamic stability using density functional theory, 103 nanowires meet per-atom and per-Ångström thermodynamic stability criteria. We illustrate for three nanowire systems that a variety of local minima can be present in these systems, demonstrating one case of a Peierls distortion. The wires display a broad diversity of electronic and magnetic properties of these nanowires, with 14 metals, 7 half-metals, and 82 semiconductors and insulators, and 41 nanowires displaying magnetic moments ranging from 0.1 to 5 μ_B per *d*-valence species when assuming ferromagnetic order. A subset of these chains are investigated for the impact of magnetic ordering, identifying 1D FeCl₃ to be most stable in an antiferromagnetic state. The electronic and magnetic properties of the identified 1D materials could enable applications in spintronic and quantum devices.

DOI: [10.1103/PhysRevMaterials.7.076002](https://doi.org/10.1103/PhysRevMaterials.7.076002)**I. INTRODUCTION**

Nanomaterials are of great scientific interest due to their unique electronic, optical, magnetic, and quantum properties [1–10]. These properties enable a variety of potential applications, including optoelectronic [6,11], spintronic [12,13], and quantum devices [14,15]. The emergence of these properties, when transitioning from bulk precursor to low-dimensional materials, stems from the enhancement of quantum mechanical effects, e.g., quantum confinement.

Nanomaterials range from zero-dimensional (0D) clusters and nanocrystals to 1D nanotubes, wires, and ribbons to 2D nanolayers. Zero-dimensional materials have been a topic of research for several decades due to the tunability of their properties with system size [2]. Nanocrystals have numerous applications, such as semiconducting quantum dots for lighting, displays, and photovoltaics [9,16,17]; metal oxide and chalcogenide nanocrystals for catalysis [18–20]; fluorescent semiconductor nanocrystals for medical imaging [21]; and functionalized silica nanoparticles for disease treatment [22].

One-dimensional materials have received less attention than other nanomaterials [23], with the main focus for this class of materials on nanotubes [24] and nanoribbons [25], both of which are synthesizable from 2D materials. However, several investigations have synthesized so-called extreme nanowires of a few Ångström to nanometer radius by encapsulating them within carbon nanotubes [3,26–30].

Two-dimensional materials became of great interest with the discovery of graphene with its unique electronic and

mechanical properties [1]. Since then, a large number of 2D materials have been predicted and discovered, such as *h*-BN [7,31], transition metal di-chalcogenides [4,8,32], MXenes [33,34], metal oxides [35,36], and phosphorene [37,38], with several reviews describing the experimental [39–41] and computational efforts [42–44].

Methods for the discovery of novel nanomaterials fall into two categories: approaches that rely on known crystal structures and approaches agnostic to prior crystal structure knowledge. Methods in the former category include data mining of crystal structure databases [45–48] and chemical substitutions in known prototype nanostructures [32,49–51]. These methods have successfully predicted 2D materials that were subsequently synthesized experimentally [5,50,52–57]. Techniques agnostic to known crystal structures include genetic algorithm and particle swarm structure searches [58–60], which use an objective function, such as the thermodynamics stability, to evaluate the fitness of the generated crystals and guide the creation of new structures. Most of these discovery efforts for nanomaterials focus on 2D nanosheets, with only a few studies identifying 1D structural motifs in bulk materials [10,48,61].

In this paper, we predict exfoliable 1D materials that fall under the category of “extreme nanowires” and characterize their stability, magnetic properties, and electronic behavior. We specifically focus on magnetic nanowires to provide materials that can be used to validate rich theoretical predictions for 1D spin chains, e.g., the long-range spin order in 1D Heisenberg or XY magnets [62–64], spin-Peierls and charge ordering transitions [65], helimagnetism, and the emergence of Majorana bound states [66,67]. We apply the topological scaling algorithm (TSA) [46,68] to search the Materials

*rhennig@ufl.edu

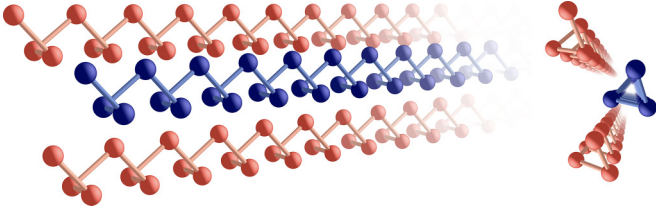


FIG. 1. The structure of bulk tellurium with a three-atom unit cell consists of 1D structural motifs, highlighted by the single chain of blue atoms. Exfoliation of such a material can lead to a 1D material, which corresponds to an inorganic polymer or nanowire. This Te nanowire forms a three-fold-symmetric helical coil, denoted as 3H-Te.

Project database [69] and classify the dimensionality of the structural motifs comprising each metastable bulk material. We identify 551 homogeneous bulk materials composed of van der Waals (vdW) bonded chains, i.e., pseudo-1D solids, which are within 50 meV atom^{-1} of the thermodynamic hull. Figure 1 illustrates, as an example, the 1D structural motif of tellurium (Te). We isolate these 1D materials and calculate their thermodynamic stability, using single-chain 3H-Te as the reference for thermodynamic stability due to its bulk precursor being the density functional theory (DFT) ground state [69] and its successful synthesis both as a nanofilm [70] and inside carbon nanotubes [3]. We proceed to investigate the electronic and magnetic properties of the stable 103 nanowires that contain transition metals. We use MoBr_3 , NbCl_3O , and HgO to demonstrate the impact of structural distortions on 1D systems and illustrate the complexity of their energy landscapes. We further show that 1D materials exhibit a wide range of electronic and magnetic properties, revealing potential pathways to electronic applications and the value of investigating this relatively unexplored class of materials in greater depth.

II. METHODS

We apply the TSA developed by Ashton *et al.* [46] and implemented in the MPInterfaces software package [68] to identify the dimensionality of the structural motifs comprising the materials in the Materials Project database. We use the empirical atomic radii [71] specified in the pymatgen software package [72] to characterize the bonding network. We employ the MPInterfaces [68] and pymatgen [72] software packages to exfoliate the isolated 1D structures, perform the DFT calculations, and analyze the results. We identify and remove duplicate 1D materials by comparing the interatomic distances of systems with identical compositions.

The DFT calculations of the stability and properties of the 1D materials are performed with the plane-wave code VASP [73] using the projector-augmented wave method [74] and the generalized gradient approximation. To account for dispersion interactions between the 1D structural motifs in the bulk structure, we employ the vdW-DF-optB88 approximation [75,76] for the exchange-correlation functional. A plane-wave cutoff energy of 600 eV, a Γ -centered k -point mesh with a density of 60 k -points \AA along the periodic directions, and a first-order Methfessel-Paxton smearing with a width of 0.1 eV

ensure convergence of the energy of the relaxed structures to better than 1 meV atom^{-1} . All calculations are performed spin polarized and initialized ferromagnetically unless otherwise stated, with d valence elements initialized with $6\mu_B$ and all other elements with $0.5\mu_B$. To improve the reliability of the structural optimization, we employ a damped molecular dynamic algorithm with a damping factor between 0.2 and 0.4 and a small time step of 0.05 to 0.3 fs. The electronic band structures were calculated using the tetrahedron method with Blöchl corrections.

We place all 1D materials in an orthorhombic simulation cell such that their periodic direction is parallel to the a axis. To determine the vacuum spacing required to converge the nanowires' energy to 1 meV atom^{-1} , we calculate the change in energy when increasing the vacuum spacing from 10 to 26 \AA for 30 randomly selected 1D materials. The dispersion interaction between two parallel metallic wires scales with distance, d , as $1/d^2$ [77]. Using this scaling relation, we find that the energy is converged to well below 1 meV atom^{-1} for a vacuum spacing of 20 \AA , which we apply to the nonperiodic directions of the nanowire cells.

III. RESULTS

A. Identification of structural motifs

We apply the TSA to identify the structural motifs of all materials contained in the Materials Project database of August 23, 2019. The creation of the bonding network in the TSA requires a choice of bond lengths. This is because the definition that the TSA uses classifies atoms as “bonded” if the radii of two species overlap. As such, as one scales the radius of each atom, the cutoff for the bonding classification between atoms is scaled. Increasing this bond length scaling results in more connected crystals, and an eventual convergence to a fully 3D crystal. The base empirical atomic radii of the species is as specified in the pymatgen software package and we scale the values from -20% to $+30\%$ in steps of 1% to identify bonds.

Figure 2 illustrates the distribution of structural motifs for all materials within 50 meV atom^{-1} of the thermodynamic hull. Unsurprisingly, the unscaled atomic radii result in the classification of the majority of crystal structures into molecular heterostructures, composed of single atom atomic clusters. To ensure accurate identification of the bonds and capture the structural motif of each crystal correctly, we increase the atomic radii by $+20\%$. This scaling generally ensures the correct identification of almost all covalent, ionic, and metallic bonds while being unlikely to include second-nearest neighbors and weak vdW bonds.

For any empirical bonding parameter, there will be a fraction of incorrectly identified materials. An example of this is layered PbS. The Pb and S species exhibit atomic radii of 1.8 and 1.0 \AA , respectively. In the PbS structure, the distance between nearest-neighbor Pb and S atoms is 3.01 \AA , which requires a minimum increase of the atomic radii of 7.5% for the TSA to identify these species as bonded. However, when increasing the radii by 8.4%, the Pb atoms of one monolayer are identified as bonded to the S atoms of the opposite layer. Though the number of misidentified structural motifs is a

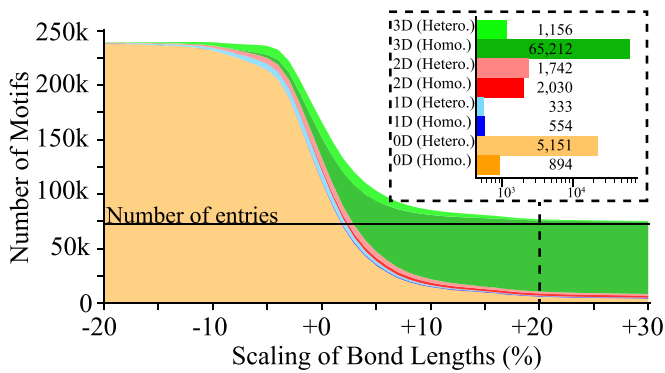


FIG. 2. Distribution of structural motifs identified by the TSA as a function of the scaling of the bond length, i.e., the sum of empirical atomic radii. The figure is limited to materials which are reported as within 50 meV atom^{-1} of the thermodynamic hull. For materials where a heterostructure was identified (i.e., the composition of individual structural motifs does not match the materials composition), each bonding network with a unique composition is categorized separately. The number of conventionally networked materials increases rapidly up to a scaling of about +10%. We select a scaling of +20% to capture almost all covalent, ionic, and metallic bonds but not bridge the majority of van der Waals gaps.

priori unknown, visual inspection of a subset of materials and the apparent convergence of the structural motifs with further increase in the scaling of the bond length indicates that the number of misidentified cases is relatively small for a scaling of +20%.

Figure 2 shows that the number of identified structural motifs is larger than the number of considered crystal structures (72,316). The reason is that some crystal structures comprise multiple structural motifs. The structural motifs of these heterostructures can differ in both their chemical composition and their dimensionality, e.g., heterostructures of 0D and 2D motifs. Across the 3,632 chemical heterostructures, 1,850 have mixed dimensionality. We do not consider chains obtained from heterostructures, as they may not be easily exfoliable. Further, they may be charged and, thus, likely unstable when isolated from the bulk precursor.

B. Bipartite structures

Though changing the supercell size should not change the structural motif of a crystal, we find several materials that display structural motifs whose identified dimensionalities depend on the supercell size chosen. For example, the monoclinic phosphorous crystal with Materials Project ID mp-568348 and Inorganic Crystal Structure Database (ICSD) [78] ID 29273 is identified as a 1D solid with a $2 \times 2 \times 2$ supercell, a 2D solid with a $3 \times 3 \times 3$ supercell, and a scaling between 1D and 2D with a $4 \times 4 \times 4$ supercell. Figure 3 displays this crystal structure and illustrates how using the same primitive cell to generate supercells can result in different identified bonding networks due to the periodic boundary condition.

Figures 3(a) and 3(b) demonstrate that this phosphorous crystal structure comprises two interwoven networks, denoted in red and blue. These networks consist of a series of rodlike

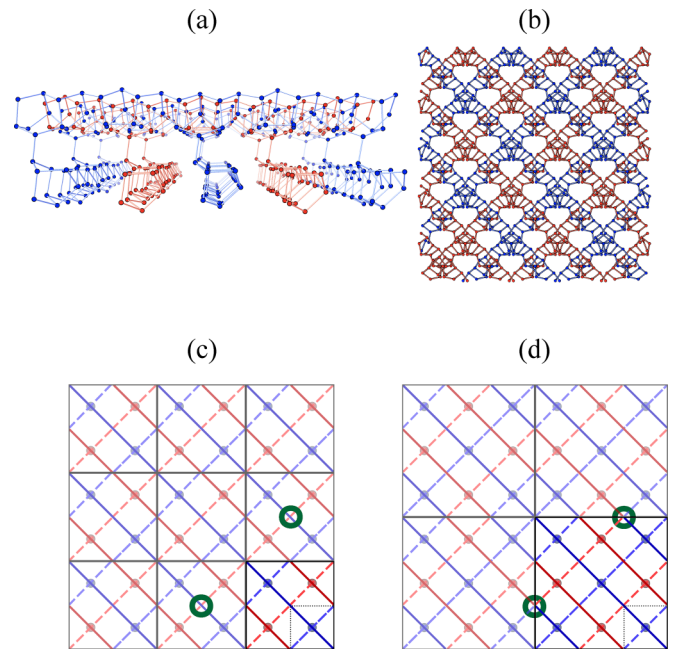


FIG. 3. Effect of periodic boundary conditions on the dimensionality of structural motifs. The phosphorous bipartite structure comprises two separate bonding networks represented in red and blue. (a) The crystal structure consists of two networks of linked rodlike motifs. The top and bottom sets of atoms form equivalent structures that are related by a 90° rotation and connected through bridging phosphorous atoms. (b) The top-down view shows the bipartite network structure. Panels (c) and (d) display 6×6 supercells of the unit cell, constructed from 2×2 and 3×3 supercells, respectively. The region within the black lines represents the primitive cell of the crystal. The dashed lines represent the bottom rods, solid lines represent the top rods, and dots represent the points at which the upper and lower rods connect. The green circles highlight the conflicting network connectivity for the 3×3 supercell (d), which shows the blue bonding network incorrectly connected to the red bonding network.

motifs in a top and bottom layer rotated by 90° angle, with bridging phosphorous atoms connecting these layers. This connectivity allows the two atomic networks to interweave, resulting in a structure with bipartite character.

Figures 3(c) and 3(d) demonstrate how the periodic boundary conditions, considering a 2×2 and 3×3 supercell, affect the identification of the structural motifs. The solid and dashed lines represent the “top” and “bottom” rods, and filled circles denote the bridging phosphorous atoms connecting these rods. The black dashed lines represent the region corresponding to the primitive cell of the material. In the case of the 3×3 supercell, the “red” bonding network continues across the periodic boundary as the “blue” bonding network, highlighted with the green circles. This incorrectly classifies the distinct atomic networks as “bonded,” an issue that is not seen at the equivalent points in the 2×2 representation. This is observed with any supercell representation, including the primitive cell, where one of the periodic directions is an odd integer supercell of the primitive cell. In the 2×2 supercell, the periodic boundary condition correctly classifies the bonding networks as interwoven but not connected.

This failure in the periodic boundary condition indicates that, e.g., transport calculations performed on such systems using an odd-sized supercell representation may result in incorrect properties. We identify 23 homogeneous crystals that display a change in the dimensionality of their structural motifs with supercell size. We define these systems as “bipartite crystals,” materials in which two or more bonded networks are interwoven but not chemically bonded. The interwoven nature of these networks can result in the distinct bonded networks being misclassified as bonded. A list of these crystals can be found in the supplementary materials [79].

C. Exfoliation and structural stability of 1D nanowires

From our starting set of 120,612 crystals, 551 crystals consist of 1D motifs and are within 50 meV atom⁻¹ of the thermodynamic hull, indicating experimental accessibility. We further focus our search on materials that include at least one *d*-valence element, as such species in low-dimensional systems have the potential for strong correlation effects, unique magnetic and charge ordering transitions, and Majorana bound states [62–67]. This results in 293 crystal structures with 1D structural motifs, which we further screen to reduce duplicates. We also remove any materials with an *f*-valence species, as these elements are not well modeled with semilocal exchange-correlation functionals in DFT. For each chemical formula, all crystals with an ICSD entry were considered. If any theoretical Materials Project crystal was lower in reported PBE energy than the ICSD phases, the most stable theoretical crystal was also considered. These criteria result in 263 crystals with 1D structural motifs considered in this work, from which we exfoliate a individual nanowires and characterize them using DFT.

After exfoliating the nanowires from the bulk precursor materials, we relax the atomic positions and the periodic lattice parameters of the structures. Noteworthy, the relaxation of the nanowires is exacerbated by local structural minima. We find that a damped molecular dynamics approach improves the convergence of the relaxations and found that perturbing the atomic positions to break the symmetry improved convergence in several cases.

Next, we determine the thermodynamic stability of each nanowire. We calculate the exfoliation energy of the isolated nanowire relative to the bulk precursor,

$$\Delta E_{\text{exf}} = \frac{E_{\text{chain}}}{N_{\text{chain}}} - \frac{E_{\text{bulk}}}{N_{\text{bulk}}}, \quad (1)$$

where E_{chain} and E_{bulk} denote the energy and N_{chain} and N_{bulk} the number of atoms in the unit cell of the isolated 1D chain and the bulk precursor structure, respectively. The exfoliation energy measures the thermodynamic stability of the 1D material against the formation of the precursor bulk phase.

We introduce a second stability criterion, which we call the line tension,

$$\sigma_{\text{exf}} = \frac{N_{\text{chain}}}{a_{\text{chain}}} \Delta E_{\text{exf}}, \quad (2)$$

where a_{chain} is the periodic lattice vector of the 1D chain structure. The line tension is a 1D analog to the surface energy of 2D materials and renormalizes the exfoliation energy by the

linear atom density of the nanowire. We find the line tension stability criterion avoids the bias of the formation energy towards larger cross-section nanomaterials, just as surface energy avoids a bias towards larger thickness nanolayers [42,58].

We use the 3H-Te nanowire with a threefold-symmetric helical coil as a reference to classify the stability of the 1D materials. Though a free-standing Te nanowire has not yet been experimentally synthesized, the thin-film precursor [70] and a 3H-Te nanowire encapsulated in a carbon nanotube have been synthesized [3]. A linear Te nanowire was theorized to exhibit a structural distortion. However, this phase was not seen in the experiments, possibly due to limitations in imaging technology [3]. We consider this possibility by generating doubled, tripled, and octupled supercells with perturbations of each atomic position by 0.1 Å along random directions. We find that all supercells relax back to the pristine 3H structure, indicating the absence of structural distortions in this system.

We note that while other nanowires have also been synthesized within carbon nanotubes [26–30], Te is the only known material identified with a thermodynamically stable bulk precursor composed of the nanowire structural motif. Sulfur exhibits a bulk phase with a 1D structural motif, and a sulfur nanowire has been encapsulated in a carbon nanotube [30]. However, the ground-state bulk structure is not composed of sulfur nanowires. Therefore, the 3H-Te nanowire, with an exfoliation energy of 441 meV atom⁻¹ and a line tension of 234 meV Å⁻¹, is the most relevant reference for the stability standard of nanowire materials. We expect the criteria for thermodynamic stability to evolve as more exfoliable nanowires are synthesized and growth techniques develop over time. Calculating the dynamic stability of these nanowires may further expand the stability criterion.

Figure 4(a) compares the line tensions and exfoliation energies for the nanowires with single-chain 3H-Te. Using the exfoliation energy of 3H-Te as the stability criterion, we observe that all considered nanowires are stable. However, using the line tension to account for the nanowire cross section, just 103 of the exfoliated nanowires are sufficiently stable, approximately 40% of the starting set of materials. Figure 4(b) compares the line tensions to the elliptical cross sections of the nanowires. Of the 103 stable nanowires, 96.1% display a cross section less than 75 Å². Of all nanowires with a cross section greater than 75 Å², only 7% (4 of 57) are stable. This indicates that the “line tension” criterion is successful in avoiding bias towards larger cross-section nanowires and is a potential 1D analog to the 2D surface energy stability criterion [42,58]. Thus, we consider these 103 nanowires viable for synthesis and further characterize them.

D. Structural distortions

Several of the 103 metastable nanowires have the same chemical compositions. These nanowires are generally similar to each other but were exfoliated from bulk precursor phases with different structures. Twenty-one chemical compositions appear twice, and one (HgO) appears four times. Some of the precursors are very similar polymorphs, providing insight into the metastability of these nanowires. The nanowires exfoliated from these polymorphs are primarily composed of a high and a low-symmetry phase.

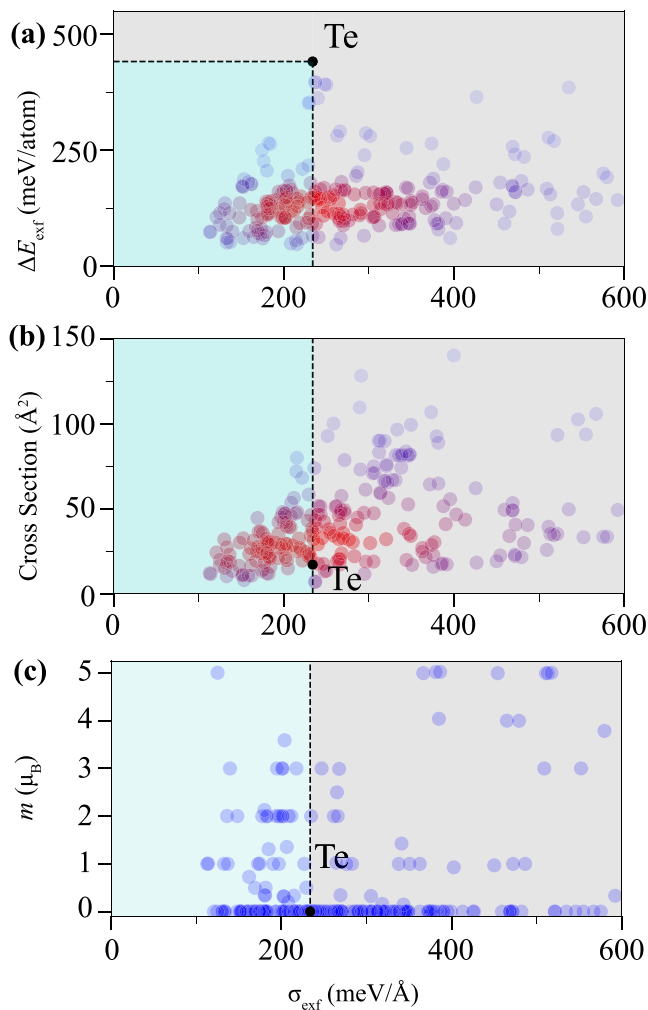


FIG. 4. Density scatter plots showing the nanowire distribution for (a) the exfoliation energy, (b) the elliptical nanowire cross section, and (c) the average magnetic moment normalized by the number of d -valence elements as a function of the line tension. The black circle represents single-chain 3H-Te, which provides an empirical stability criterion indicated by the light blue region.

Next, we discuss three examples of structural distortions in exfoliated nanowires, illustrated in Fig. 5. While the exfoliation energy is appropriate when considering the synthesis from a bulk precursor, properly comparing the stability of nanowires exfoliated from different bulk precursors with the same composition requires a common reference. As such, we reference the crystal on the thermodynamic hull, i.e., the most stable crystal in the thermodynamic energy landscape for a given chemical composition. We use stability criteria with the common reference of the energy of the convex hull,

$$\Delta E_{\text{hull}} = \frac{E_{\text{chain}}}{N_{\text{chain}}} - \frac{E_{\text{hull}}}{N_{\text{hull}}}, \quad (3)$$

and the line tension,

$$\sigma_{\text{hull}} = \frac{N_{\text{chain}}}{a_{\text{chain}}} \Delta E_{\text{hull}}, \quad (4)$$

where E_{hull} denotes the energy and N_{hull} the number of atoms of the structure on the thermodynamic hull. In the case of the

example chemical systems, the crystal on the thermodynamic hull of each composition is the parent crystal of nanowires D-MoBr₃, D-NbCl₃O, and ZZ-HgO.

The first nanowire is molybdenum tribromide (MoBr₃), which demonstrates that shallow energy landscapes can occur for some 1D materials. While the structural-distorted wire in Fig. 5(b) (D-MoBr₃, space group 25 P_{2mm}) has a higher exfoliation energy, it is 17 meV atom⁻¹ more stable than the more symmetric wire in Fig. 5(a) (S-MoBr₃, space group 51 P_{amm}). This is due to the D-MoBr₃ bulk precursor being on the thermodynamic hull, resulting in a nanowire that requires more energy to exfoliate but is closer to the system's ground state. The lattice parameter of the lower energy D-MoBr₃ is 6.08 Å with alternating Mo-Br-Mo angles of 65.4° and 77.9°, while the high-energy S-MoBr₃ has a lattice parameter of 5.99 Å and equal Mo-Br-Mo angles of 70.4°. When breaking the inversion symmetry of S-MoBr₃, the nanowire relaxes to the distorted low-energy D-MoBr₃ structure. This break in symmetry also results in a metal-insulator transition, with the net magnetic moment of the Mo₂Br₆ formula unit transitioning from 4.2- to 4.0-bohr magnetons, making the structural distortion a Peierls distortion.

The second example is niobium oxychloride (NbCl₃O), which displays an even smaller exfoliation energy difference between nanowire polymorphs. Like MoBr₃, NbCl₃O has a symmetric nanowire (S-NbCl₃O, space group 65 C_{mmm}) and a symmetry-broken distortion of said nanowire (D-NbCl₃O, space group 35 C_{2mm}), shown in Figs. 5(c) and 5(d), respectively. This does not result in a metal-insulator transition, however, meaning that the distortion would not be qualified as a “Peierls” distortion. The bulk precursor of the distorted wire is again the thermodynamic ground state of the composition. Comparing both nanowires to this reference phase, S-NbCl₃O is less stable by 15 meV atom⁻¹ than D-NbCl₃O. In this system, breaking the mirror plane perpendicular to the nanowire axis allows the Nb-Cl bonds to tilt and results in the extension of the Nb-O bonds.

The final example is mercury oxide (HgO). Though all four HgO nanowires exfoliated from four different bulk precursors are unstable relative to 3H-Te, the system illustrates different ordering for the two stability criteria relative to the bulk ground state. As exfoliated, two of the nanowires contain three formula units and are threefold helical (3H), while the other two contain two formula units and exhibit a linear zigzag structure. After optimization, each 3H nanowire relaxes to different local minima of with lattice parameters of 9.49 and 9.38 Å shown in Figs. 5(f) and 5(g) and similar energy while the linear zigzag nanowires relax to the same minimum illustrated in Fig. 5(e). These three HgO nanowires shown in Figs. 5(e), 5(f), and 5(g) have formation energies, ΔE_{hull} , of 397, 393, and 394 meV atom⁻¹, respectively, and line tensions, σ_{hull} , of 237, 249, and 252 meV Å⁻¹, respectively. The bulk precursor associated with the zigzag nanowire is the most stable, though the least stable precursor is only 2.5 meV atom⁻¹ above the thermodynamic hull. The line tension σ_{hull} is lowest in the zigzag phase, while the hull distance ΔE_{hull} is lower in the 3H nanowires. This shows that there is no universal agreement between these two stability criteria, and thus stability criteria for 1D materials are likely to evolve as the field develops.

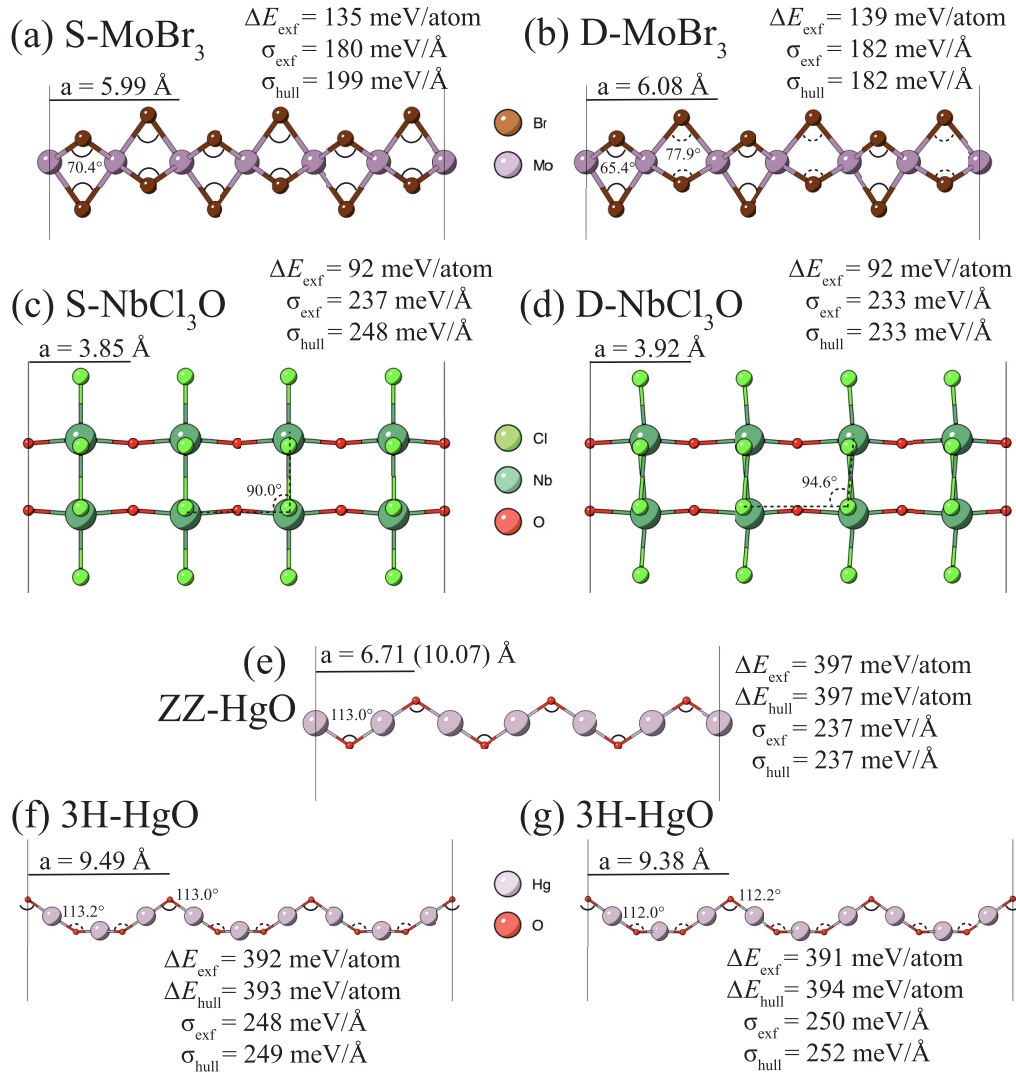


FIG. 5. Examples of structural distortions observed in this work. These correspond to [(a) and (b)] MoBr_3 , [(c) and (d)] NbCl_3O , and [(e) and (f)] HgO . The low-energy phase of MoBr_3 and NbCl_3O are shown in (b) and (d), respectively. The lowest-energy HgO nanowires differ for the exfoliation energy and line tension stability criteria.

These examples demonstrate the potential for these nanowires to exhibit multiple structures of similar energy. The small energy differences indicate the possibility of phase transformations between the symmetric and distorted structures at higher temperatures, affecting their properties. We reiterate that part of the relaxation framework was perturbing atomic positions of structures that did not converge during relaxation. This suggests that some nanowires exhibit a structural distortion that is not present in the bulk precursor.

E. Electronic structures

Figure 6 compares the spin gaps of the nanowires obtained with the PBE functional. The large variety of electronic structures indicates the potential of nanowires for different applications. The 103 nanowires comprise 14 metals, 7 half-metals, and 82 semiconductors and insulators. Among the 82 stable semiconducting and insulating nanowires, we identify 15 straddling, 9 staggered, and no broken spin-gap insulating nanowires. We also check for the potential for equally sized

spin gaps which do not align their band edges but identified no such materials. Seven half-metallic (16 insulating) nanowires display a metallic channel (lesser band gap), which is the majority electron spin channel.

The PBE functional typically underestimates the band gap, and hybrid functionals or many-body GW calculations may be required to accurately ascertain the band gap and half-metallic character of these nanowires [80]. Furthermore, Peierls distortions could affect the electronic structure and open a gap in the metallic and half-metallic systems. Nevertheless, we expect that the results provide a first screening step and motivate more detailed future studies of specific nanowires.

F. Magnetic nanowires

Figure 4(c) compares the magnetic moments of the exfoliated nanowires. We consider magnetic nanowires with a minimum magnetic moment per magnetic d species of 0.1-bohr magneton (μ_B) and identify 41 magnetic 1D materials, 27 of which display integer magnetic moments per unit cell.

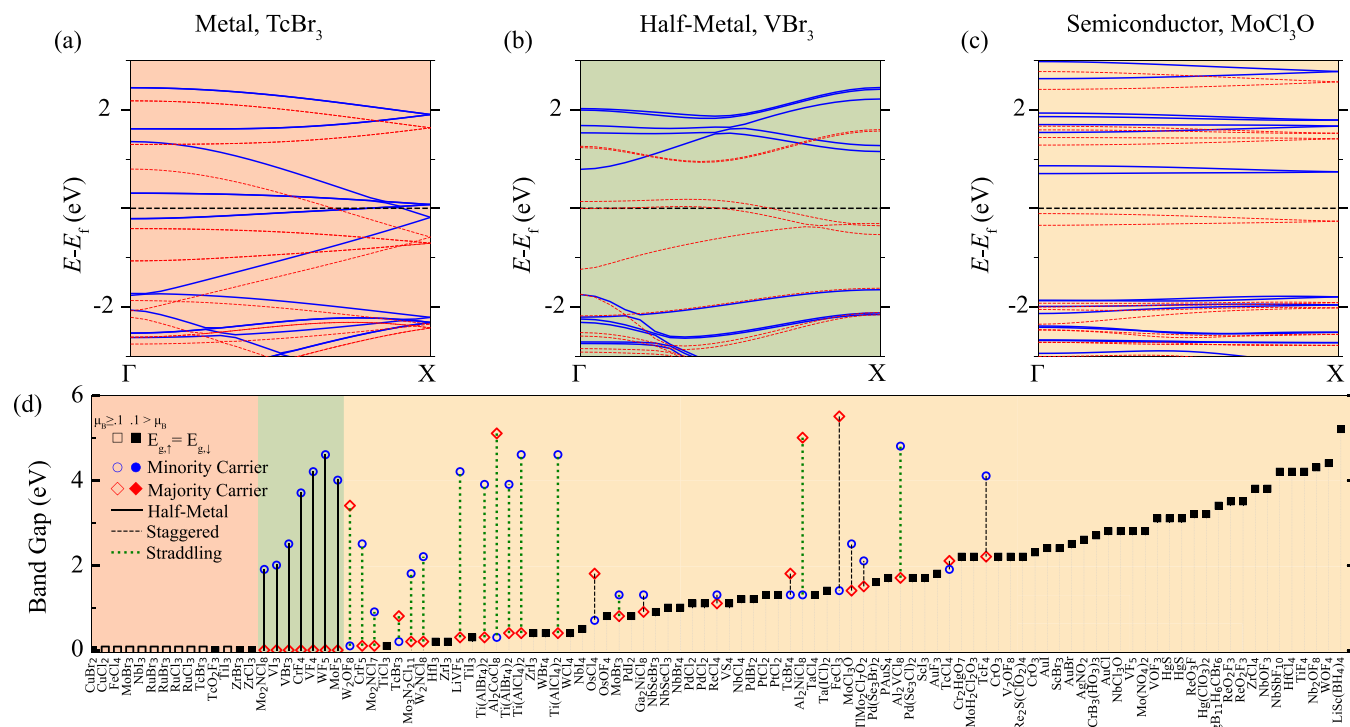


FIG. 6. Electronic structure of the stable nanowires. The nanowires exhibit a variety of electronic structures, illustrated by the band structure of (a) metallic $TcBr_3$, (b) half-metallic VBr_3 , and semiconducting MoI_3O with the spin channels denoted by solid blue and dashed red lines. (d) The 103 identified stable nanowires comprise 14 metals, 7 half-metals, and 82 semiconductors and insulators, shown in order of increasing band gap. The red diamonds (blue circles) indicate that the spin channel corresponds to the majority (minority) electron carrier. Black squares indicate both band gaps are equal, with magnetic (nonmagnetic) nanowires are shown with an empty (filled) markers. Metals are ordered alphabetically and half-metals/insulators are ordered by band gap. The red, green, and orange shadings indicate metallic, half-metallic, and semiconducting nanowires, such as shown in the example band structures [(a)–(c)]. Staggered-gap and straddling-gap insulators are plotted with dashed black and dotted green lines, respectively.

We also observe nanowires where only some d valence species contribute to the magnetic behavior (e.g., $AgTa_2F_{12}$ with $1\mu_B$ per formula unit), though this is uncommon.

To investigate the possibility of different magnetic ordering and structural distortions, we select the nanowire with the lowest exfoliation energy for each integer magnetic moment for further characterization. The bulk precursor of each nanowire has the same net μ_B per d species as the nanowires when assumed to have ferromagnetic ordering. First, we calculate the energy for ferromagnetic (FM), nonmagnetic (NM), and antiferromagnetic (AFM) orderings of alternating moments (+ - + -) and paired moments (+ + - -) along the chain. Second, we test for structural distortions in the FM configuration by doubling and tripling the chain length, perturbing atomic positions by 0.1 \AA along random directions, and reoptimizing the structures.

Table I shows how the magnetic order and potential structural distortions affect the stability measured by the line tension for the five selected nanowires with the lowest exfoliation energy for each integer magnetic moment. First, all five nanowires prefer a magnetic state over a nonmagnetic one. Second, we find that four of the five nanowires have no strong preference for any specific magnetic order, indicating a small exchange coupling between the magnetic moments. The $FeCl_3$ nanowire shows a significant preference for an alternating + - + - AFM order, with one magnetic Fe atom

per primitive cell. This corresponds to an energy gain of 104 meV per Fe ion. Only one system ($TcCl_4$) prefers a paired + + - - AFM ground state, though the thermodynamic stability gained is only 2 meV \AA^{-1} . The tripled FM cell of the $FeH_4C_2O_6$ nanowire was relaxed twice, with two different applied atomic perturbations. One calculation lead to the same energy as the ferromagnetic $1 \times$ and $2 \times$ supercells. The other calculation lead to a ground state 18 meV \AA^{-1} greater than

TABLE I. Stability measure by line tension σ_{exf} in units of meV \AA^{-1} and magnetic moment, M , in units of μ_B per d element, of several magnetic 1D nanowires for multiple magnetic configurations. The FM configuration is shown for individual, doubled, and tripled unit cells. Two AFM configurations were considered, with alternating (+ - + -) and paired (+ + - -) moments. The NM configurations are the least stable in all cases.

	Ferromagnetic			AFM		NM	
	M	$1 \times$	$2 \times$	$3 \times$	+ - + -		+ + - -
MoF_5	1	116	116	116	114	118	144
$TiAl_2Cl_4$	2	198	198	197	197	198	332
$TcCl_4$	3	195	195	195	193	191	378
$FeH_4C_2O_6$	4	385	384	385	386	387	462
$FeCl_3$	5	126	126	128	98	110	454

the ferromagnetic systems with a compressed unit cell (15.9 vs. 16.2 Å). This again demonstrates that the energy landscape of nanowires is complex and that computational investigations of 1D systems require consideration of the interplay between potential structural distortions and magnetic ordering.

These results illustrate the rich diversity of the magnetic properties of 1D nanowires and the challenges and opportunities that may be encountered. While isolating single nanowires is a significant challenge, monolayers composed of a series of vdW bonded nanowires may produce the benefits of anisotropic transport and magnetic properties with less difficulty. Dramatically anisotropic magnetotransport has been observed in a monolayer of vdW bonded 3H-Te wires [70], indicating the possibility of other nanowires having highly anisotropic properties in the more easily achieved monolayer form. The Mermin-Wagner theorem states that long-range magnetic order cannot exist in isotropic 1D or 2D systems [62]. However, 2D Ising magnets have been theoretically predicted and experimentally observed, such as in 2D Fe₃GeTe₂ [5,54,55]. There is also a significant amount of research on the periodicity of magnetism in cylindrical nanowires, constructed using unit cells of conventional bulk crystals with varying radii [81]. This indicates the possibility for long-range magnetic order in 1D extreme nanowires for sufficiently strong magnetocrystalline anisotropy energy.

IV. CONCLUSION

In summary, the Materials Project database was searched for novel 1D materials using the Topological Scaling Algorithm. A cutoff of 120% of the atomic radius was considered for building the bonded network graphs, resulting in 551 materials within 50 meV atom⁻¹ of the thermodynamic hull exhibiting 1D structural motifs. Among them are 293 materials containing *d*-valence elements, with a potential for strong electron correlations, and were studied in this work. Nanowires are exfoliated from the 263 bulk crystals that either have an ICSD entry or are closest to the thermodynamic hull. We relaxed these nanowires and calculated their thermodynamic stability using the exfoliation energy and line tension. We used single-chain tellurium as the benchmark of stability and found that nearly all the chains fulfill the exfoliation energy criterion, while only 103 fulfill the line tension criterion, which we select as the stability criterion. We observe a diverse spectrum of electronic and magnetic states for these extreme nanowires with 14 metals, 7 half-metals, and 82 insulators. For five semiconducting nanowires, we investigate the mag-

netic ordering in detail. One system had a strong preference for ferromagnetic ordering, and four systems had a maximum stability difference of 4 meV Å⁻¹ between magnetic configurations.

We note that analysis of dynamic stability, i.e., the verification of all phonon modes being real, was not performed in this screening. While exfoliation from a stable bulk precursor indicates that the nanowires will also be dynamically stable, the nanowires can still undergo structural distortions, as observed in this work in MoBr₃, NbCl₃O, and HgO. Further, there is the potential for coiling and bending in free-standing nanowires with large-enough periodic boundary conditions. As such, individual nanowires of interest should have their phonon spectra calculated to ensure dynamic stability before investigated further.

Future investigations into these materials should focus on the magnetocrystalline anisotropy, magnetic ordering, and exchange coupling of the extreme nanowires to provide insight into their potential use in electronic and quantum applications. Further, determining the source and consequences of structural distortions in these systems could provide insight into the physics behind inorganic polymers and improve predictions of distortion-driven phase transformations. An additional consideration would be the change in properties when forming a monolayer of a given nanowire, which may be more experimentally accessible than isolated nanowires. Finally, while the line tension stability criterion provides a valuable metric to screen nanowires with a range of cross sections, further work is required to better understand the energy landscape of 1D materials. Data from this work are available on the MaterialsCloud Archive repository [82] and the supplementary material of this work [79].

ACKNOWLEDGMENTS

This work was performed under National Science Foundation Grant No. PHY-1549132, the Center for Bright Beams, and the UF Informatics Institute. S.R.X. and R.G.H. acknowledge support from Basic Energy Sciences, United States Department of Energy, Contract No. DE-SC0020385. This research was performed using the computational resources of the University of Florida Research Computing Center. Part of this research was performed while the author was visiting the Institute for Pure and Applied Mathematics (IPAM), which is supported by the National Science Foundation under Grant No. DMS-1440415.

-
- [1] K. S. Novoselov, A. K. Geim, S. V. Morozov, D. Jiang, Y. Zhang, S. V. Dubonos, I. V. Grigorieva, and A. A. Firsov, *Science* **306**, 666 (2004).
 - [2] A. P. Alivisatos, *Science* **271**, 933 (1996).
 - [3] P. V. C. Medeiros, S. Marks, J. M. Wynn, A. Vasylenko, Q. M. Ramasse, D. Quigley, J. Sloan, and A. J. Morris, *ACS Nano* **11**, 6178 (2017).
 - [4] K. F. Mak, C. Lee, J. Hone, J. Shan, and T. F. Heinz, *Phys. Rev. Lett.* **105**, 136805 (2010).
 - [5] Y. Deng, Y. Yu, Y. Song, J. Zhang, N. Z. Wang, Z. Sun, Y. Yi, Y. Z. Wu, S. Wu, J. Zhu, and J. Wang, *Nature (London)* **563**, 94 (2018).
 - [6] Q. H. Wang, K. Kalantar-Zadeh, A. Kis, J. N. Coleman, and M. S. Strano, *Nat. Nanotechnol.* **7**, 699 (2012).
 - [7] G. Cassabois, P. Valvin, and B. Gil, *Nat. Photon.* **10**, 262 (2016).
 - [8] A. Splendiani, L. Sun, Y. Zhang, T. Li, J. Kim, C.-Y. Chim, G. Galli, and F. Wang, *Nano Lett.* **10**, 1271 (2010).
 - [9] K. Bourzac, *Nature (London)* **493**, 283 (2013).

- [10] Y. Zhu, D. A. Rehn, E. R. Antoniuk, G. Cheon, R. Freitas, A. Krishnapriyan, and E. J. Reed, *ACS Nano* **15**, 9851 (2021).
- [11] J. Lee, J. Huang, B. G. Sumpter, and M. Yoon, *2D Mater.* **4**, 021016 (2017).
- [12] W. Han, *APL Mater.* **4**, 032401 (2016).
- [13] D. Pesin and A. H. MacDonald, *Nat. Mater.* **11**, 409 (2012).
- [14] X. Qian, J. Liu, L. Fu, and J. Li, *Science* **346**, 1344 (2014).
- [15] J. R. Schaibley, H. Yu, G. Clark, P. Rivera, J. S. Ross, K. L. Seyler, W. Yao, and X. Xu, *Nat. Rev. Mater.* **1**, 16055 (2016).
- [16] X. Lan, O. Voznyy, F. P. García de Arquer, M. Liu, J. Xu, A. H. Proppe, G. Walters, F. Fan, H. Tan, M. Liu, Z. Yang, S. Hoogland, and E. H. Sargent, *Nano Lett.* **16**, 4630 (2016).
- [17] C. R. Bealing, W. J. Baumgardner, J. J. Choi, T. Hanrath, and R. G. Hennig, *ACS Nano* **6**, 2118 (2012).
- [18] W. T. Hong, M. Risch, K. A. Stoerzinger, A. Grimaud, J. Suntivich, and Y. Shao-Horn, *Energy Environ. Sci.* **8**, 1404 (2015).
- [19] M. S. Kodaimati, S. Lian, G. C. Schatz, and E. A. Weiss, *Proc. Natl. Acad. Sci. U.S.A.* **115**, 8290 (2018).
- [20] A. Nelson, K. E. Fritz, S. Honrao, R. G. Hennig, R. D. Robinson, and J. Suntivich, *J. Mater. Chem. A* **4**, 2842 (2016).
- [21] X. Michalet, F. F. Pinaud, L. A. Bentolila, J. M. Tsay, S. Doose, J. J. Li, G. Sundaresan, A. M. Wu, S. S. Gambhir, and S. Weiss, *Science* **307**, 538 (2005).
- [22] F. Chen, K. Ma, M. Benezra, L. Zhang, S. M. Cheal, E. Phillips, B. Yoo, M. Pauliah, M. Overholtzer, P. Zanzonico, S. Sequeira, M. Gonen, T. Quinn, U. Wiesner, and M. S. Bradbury, *Chem. Mater.* **29**, 8766 (2017).
- [23] Y. Xia, P. Yang, Y. Sun, Y. Wu, B. Mayers, B. Gates, Y. Yin, F. Kim, and H. Yan, *Adv. Mater.* **15**, 353 (2003).
- [24] E. T. Thostenson, Z. Ren, and T.-W. Chou, *Compos. Sci. Technol.* **61**, 1899 (2001).
- [25] S. Dutta and S. K. Pati, *J. Mater. Chem.* **20**, 8207 (2010).
- [26] C. E. Giusca, V. Stolojan, J. Sloan, F. Börrnert, H. Shiozawa, K. Sader, M. H. Rummeli, B. Büchner, and S. R. P. Silva, *Nano Lett.* **13**, 4020 (2013).
- [27] R. Carter, J. Sloan, A. I. Kirkland, R. R. Meyer, P. J. D. Lindan, G. Lin, M. L. H. Green, A. Vlandas, J. L. Hutchison, and J. Harding, *Phys. Rev. Lett.* **96**, 215501 (2006).
- [28] C. A. Slade, A. M. Sanchez, and J. Sloan, *Nano Lett.* **19**, 2979 (2019).
- [29] A. Vasylenko, S. Marks, J. M. Wynn, P. V. C. Medeiros, Q. M. Ramasse, A. J. Morris, J. Sloan, and D. Quigley, *ACS Nano* **12**, 6023 (2018).
- [30] T. Fujimori, A. Morelos-Gómez, Z. Zhu, H. Muramatsu, R. Futamura, K. Urita, M. Terrones, T. Hayashi, M. Endo, S. Young Hong, Y. Chul Choi, D. Tománek, and K. Kaneko, *Nat. Commun.* **4**, 2162 (2013).
- [31] D. Pacilé, J. C. Meyer, Ç. Ö. Girit, and A. Zettl, *Appl. Phys. Lett.* **92**, 133107 (2008).
- [32] C. Ataca, H. Sahin, and S. Ciraci, *J. Phys. Chem. C* **116**, 8983 (2012).
- [33] J. Halim, S. Kota, M. R. Lukatskaya, M. Naguib, M.-Q. Zhao, E. J. Moon, J. Pitock, J. Nanda, S. J. May, Y. Gogotsi, and M. W. Barsoum, *Adv. Funct. Mater.* **26**, 3118 (2016).
- [34] M. Ashton, K. Mathew, R. G. Hennig, and S. B. Sinnott, *J. Phys. Chem. C* **120**, 3550 (2016).
- [35] M. Osada and T. Sasaki, *J. Mater. Chem.* **19**, 2503 (2009).
- [36] X. Yang, Y. Makita, Z.-h. Liu, K. Sakane, and K. Ooi, *Chem. Mater.* **16**, 5581 (2004).
- [37] A. Khandelwal, K. Mani, M. H. Karigerasi, and I. Lahiri, *Mater. Sci. Eng. B* **221**, 17 (2017).
- [38] A. H. Woomer, T. W. Farnsworth, J. Hu, R. A. Wells, C. L. Donley, and S. C. Warren, *ACS Nano* **9**, 8869 (2015).
- [39] P. Miro, M. Audiffred, and T. Heine, *Chem. Soc. Rev.* **43**, 6537 (2014).
- [40] V. Singh, D. Joung, L. Zhai, S. Das, S. I. Khondaker, and S. Seal, *Prog. Mater. Sci.* **56**, 1178 (2011).
- [41] A. Gupta, T. Sakthivel, and S. Seal, *Prog. Mater. Sci.* **73**, 44 (2015).
- [42] J. T. Paul, A. K. Singh, Z. Dong, H. Zhuang, B. C. Revard, B. Rijal, M. Ashton, A. Linscheid, M. Blonsky, D. Gluhovic, J. Guo, and R. G. Hennig, *J. Phys.: Condens. Matter* **29**, 473001 (2017).
- [43] H. L. Zhuang and R. G. Hennig, *JOM* **66**, 366 (2014).
- [44] A. K. Singh, K. Mathew, H. L. Zhuang, and R. G. Hennig, *J. Phys. Chem. Lett.* **6**, 1087 (2015).
- [45] S. Lebègue, T. Björkman, M. Klintonberg, R. M. Nieminen, and O. Eriksson, *Phys. Rev. X* **3**, 031002 (2013).
- [46] M. Ashton, J. Paul, S. B. Sinnott, and R. G. Hennig, *Phys. Rev. Lett.* **118**, 106101 (2017).
- [47] G. Cheon, K.-A. N. Duerloo, A. D. Sendek, C. Porter, Y. Chen, and E. J. Reed, *Nano Lett.* **17**, 1915 (2017).
- [48] N. Mounet, M. Gibertini, P. Schwaller, D. Campi, A. Merkys, A. Marrazzo, T. Sohier, I. E. Castelli, A. Cepellotti, G. Pizzi, and N. Marzari, *Nat. Nanotechnol.* **13**, 246 (2018).
- [49] H. Şahin, S. Cahangirov, M. Topsakal, E. Bekaroglu, E. Akturk, R. T. Senger, and S. Ciraci, *Phys. Rev. B* **80**, 155453 (2009).
- [50] H. L. Zhuang and R. G. Hennig, *Appl. Phys. Lett.* **101**, 153109 (2012).
- [51] H. L. Zhuang, A. K. Singh, and R. G. Hennig, *Phys. Rev. B* **87**, 165415 (2013).
- [52] A. K. Singh and R. G. Hennig, *Appl. Phys. Lett.* **105**, 051604 (2014).
- [53] Z. Y. A. Balushi, K. Wang, R. K. Ghosh, R. A. Vilá, S. M. Eichfeld, J. D. Caldwell, X. Qin, Y.-C. Lin, P. A. DeSario, G. Stone, S. Subramanian, D. F. Paul, R. M. Wallace, S. Datta, J. M. Redwing, and J. A. Robinson, *Nat. Mater.* **15**, 1166 (2016).
- [54] H. L. Zhuang, P. R. C. Kent, and R. G. Hennig, *Phys. Rev. B* **93**, 134407 (2016).
- [55] Z. Fei, B. Huang, P. Malinowski, W. Wang, T. Song, J. Sanchez, W. Yao, D. Xiao, X. Zhu, A. F. May, and W. Wu, *Nat. Mater.* **17**, 778 (2018).
- [56] S. Liu, X. Yuan, Y. Zou, Y. Sheng, C. Huang, E. Zhang, J. Ling, Y. Liu, W. Wang, C. Zhang, J. Zou, K. Wang, and F. Xiu, *npj 2D Mater. Appl.* **1**, 30 (2017).
- [57] X. Zhou, B. Brzostowski, A. Durajski, M. Liu, J. Xiang, T. Jiang, Z. Wang, S. Chen, P. Li, Z. Zhong, A. Drzewiński, M. Jarosik, R. Szcześniak, T. Lai, D. Guo, and D. Zhong, *J. Phys. Chem. C* **124**, 9416 (2020).
- [58] B. C. Revard, W. W. Tipton, A. Yesypenko, and R. G. Hennig, *Phys. Rev. B* **93**, 054117 (2016).
- [59] X. Wu, J. Dai, Y. Zhao, Z. Zhuo, J. Yang, and X. C. Zeng, *ACS Nano* **6**, 7443 (2012).
- [60] A. K. Singh, B. C. Revard, R. Ramanathan, M. Ashton, F. Tavazza, and R. G. Hennig, *Phys. Rev. B* **95**, 155426 (2017).
- [61] P. M. Larsen, M. Pandey, M. Strange, and K. W. Jacobsen, *Phys. Rev. Mater.* **3**, 034003 (2019).

- [62] N. D. Mermin and H. Wagner, *Phys. Rev. Lett.* **17**, 1133 (1966).
- [63] P. Bruno, *Phys. Rev. Lett.* **87**, 137203 (2001).
- [64] D. Loss, F. L. Pedrocchi, and A. J. Leggett, *Phys. Rev. Lett.* **107**, 107201 (2011).
- [65] A. Vasiliev, O. Volkova, E. Zvereva, and M. Markina, *npj Quant. Mater.* **3**, 18 (2018).
- [66] Y. Kim, M. Cheng, B. Bauer, R. M. Lutchyn, and S. Das Sarma, *Phys. Rev. B* **90**, 060401(R) (2014).
- [67] S. A. Díaz, J. Klinovaja, D. Loss, and S. Hoffman, *Phys. Rev. B* **104**, 214501 (2021).
- [68] K. Mathew, A. K. Singh, J. J. Gabriel, K. Choudhary, S. B. Sinnott, A. V. Davydov, F. Tavazza, and R. G. Hennig, *Comput. Mater. Sci.* **122**, 183 (2016).
- [69] A. Jain, S. P. Ong, G. Hautier, W. Chen, W. D. Richards, S. Dacek, S. Cholia, D. Gunter, D. Skinner, G. Ceder, and K. A. Persson, *APL Mater.* **1**, 011002 (2013).
- [70] Y. Du, G. Qiu, Y. Wang, M. Si, X. Xu, W. Wu, and P. D. Ye, *Nano Lett.* **17**, 3965 (2017).
- [71] J. C. Slater, *J. Chem. Phys.* **41**, 3199 (1964).
- [72] S. P. Ong, W. D. Richards, A. Jain, G. Hautier, M. Kocher, S. Cholia, D. Gunter, V. L. Chevrier, K. A. Persson, and G. Ceder, *Comput. Mater. Sci.* **68**, 314 (2013).
- [73] G. Kresse and J. Furthmüller, *Phys. Rev. B* **54**, 11169 (1996).
- [74] P. E. Blöchl, *Phys. Rev. B* **50**, 17953 (1994).
- [75] J. Klimeš, D. Bowler, and A. Michaelides, *J. Phys.: Condens. Matter* **22**, 022201 (2010).
- [76] J. Klimeš, D. R. Bowler, and A. Michaelides, *Phys. Rev. B* **83**, 195131 (2011).
- [77] A. J. Misquitta, J. Spencer, A. J. Stone, and A. Alavi, *Phys. Rev. B* **82**, 075312 (2010).
- [78] D. Zagorac, H. Müller, S. Ruehl, J. Zagorac, and S. Rehme, *J. Appl. Crystallogr.* **52**, 918 (2019).
- [79] See Supplemental Material at <http://link.aps.org/supplemental/10.1103/PhysRevMaterials.7.076002> for a list of the MP-IDs of the bipartite crystals identified in this work; for a .yaml file containing the exfoliation energy, line tension, averaged magnetic moment, and POSCAR format structure for each nanowire identified in this work.
- [80] M. Ashton, D. Gluhovic, S. B. Sinnott, J. Guo, D. A. Stewart, and R. G. Hennig, *Nano Lett.* **17**, 5251 (2017).
- [81] C. Bran, J. A. Fernandez-Roldan, R. P. del Real, A. Asenjo, O. Chubykalo-Fesenko, and M. Vazquez, *Nanomaterials* **11**, 600 (2021).
- [82] J. Paul, J. Lu, S. Shah, S. Xie, and R. Hennig, *Materials Cloud Archive* **2022.73** (2022).